Hybrid integrated mode-locked laser using a GaAs-based 1064 nm gain chip and a SiN external cavity

EWOUD VISSERS,[1,2,*] STIJN POELMAN,[1,2] HANS WENZEL,[3] HEIKE CHRISTOPHER,[3] KASPER VAN GASSE,[1,2] ANDREA KNIGGE,[3] AND BART KUYKEN[1,2]

[1] *Photonics Research Group, Department of Information Technology, Ghent University IMEC, Ghent, B-9000, Belgium*
[2] *Center for Nano- and Biophotonics (NB-Photonics), Ghent University, Ghent, Belgium*
[3] *Ferdinand-Braun-Institut (FBH), Gustav-Kirchhoff-Str. 4, 12489 Berlin, Germany*
[*] *Ewoud.Vissers@UGent.be*

Abstract: External cavity mode-locked lasers could be used as comb sources for high volume application such as LIDAR and dual comb spectroscopy. Currently demonstrated chip scale integrated mode-locked lasers all operate in the C-band. In this paper, a hybrid-integrated external cavity mode-locked laser working at 1064 nm is demonstrated, a wavelength beneficial for optical coherence tomography or Raman spectroscopy applications. Additionally, optical injection locking is demonstrated, showing an improvement in the optical linewidth, and an increased stability of the comb spectrum.

1. Introduction

Frequency combs can be used for applications such as LIDAR [1], high speed dual comb spectroscopy [2], astronomical spectrograph calibration [3], optical coherence tomography (OCT) [4] or coherent Raman spectro-imaging [5]. The wavelength of 1064 nm is a desirable wavelength for ophthalmic OCT systems, due to it being in a dip in the absorption spectrum of ocular media [6]. For Raman spectroscopy, the wavelength of 1064 can be benificial because it reduces fluorescence compared to lower wavelengths [7]. By using a semiconductor chip based frequency comb, both the size and the costs of current systems could be significantly reduced [8].

Currently, three main types of chip based combs have emerged: Kerr combs, electro-optic combs, and mode-locked laser combs [9]. Kerr combs are generated by pumping a high-Q ring resonator with a single wavelength pump, the Kerr-nonlinearity then generates sidebands [10]. For electro-optic combs, sidebands are generated by phase modulating the light of a single frequency laser. By placing the modulator in a resonator, the sideband modulation can be cascaded, to create wide frequency combs [11]. Mode-locked lasers inherently create a comb spectrum, without the need for a single frequency laser or modulators [12].
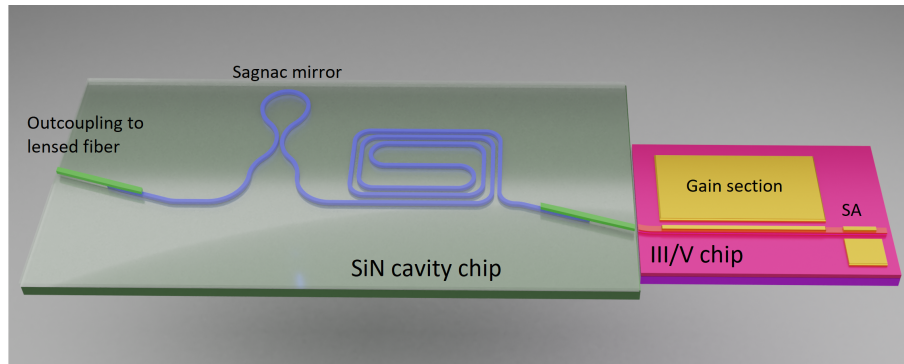
Current state-of-the-art integrated mode-locked lasers (MLL) use an external cavity design, where an active gain section is combined with a passive low-loss waveguide cavity. This technique enables scaling to repetition rates below 10 GHz, and also increases the photon lifetime in the cavity due to the low loss as, e.g., compared to InP waveguides. If the external cavity is made from a material with a low thermo-optic coefficient, the cavity length fluctuations caused by thermal noise will also be reduced. For this reason, SiN is a good candidate [13]. This increased photon lifetime leads to better fundamental noise performance [14]. To combine the active and passive sections using chip-based technology, either heterogeneous or hybrid integration has been used in many recent demonstrations [15–22].

The highest averaged outcoupled power achieved in these MLL's is 1.7 mW [19] at 2 GHz repetition rate. By increasing the saturation energy in the semiconductor optical amplifer (SOA), the output power of the laser can be increased. To achieve this, the electric field intensity in the quantum wells of the gain medium can be reduced, by increasing the mode size, or reducing the confinement for a similar mode-size.

In this paper, the same laser design and cavity fabrication technology as demonstrated in [15] are used, but a different reflective semiconductor optical amplifier (RSOA) chip is used. The SOA has a higher saturation energy, and a lower wavelength of 1064 nm instead of 1550 nm.
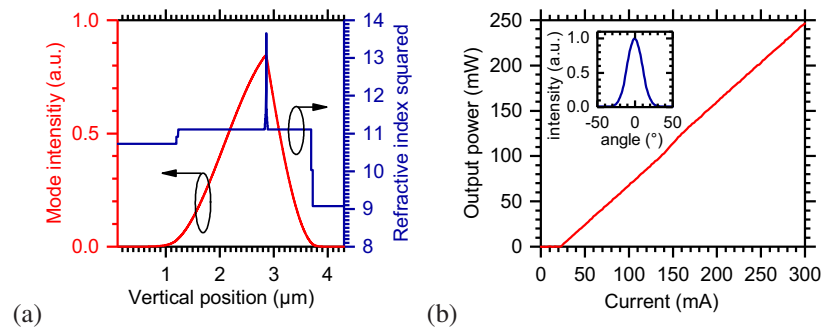
2. Design and fabrication

The laser is made from two different chips, that are hybridly integrated by butt-coupling the angled waveguide facets after fabrication as shown in Fig. 1. The butt-coupling can be done either by using a dynamic, non-permanent setup, or by permanently fixing them in a packaging process. For this demonstration, a dynamic setup was used, since it allows faster prototyping and lower costs. One of the two chips is the gain chip, made of an active material, and used for the light amplification in the laser. The second chip is the external cavity chip, used to increase the laser cavity length while keeping optical losses low.

Fig. 1. Schematic overview of the laser, with the SiN external cavity on the left in green, and the active III/V gain chip on the right in pink. Outcoupling is done with a lensed fiber from the left side of the image.

The GaAs-based asymmetric large optical cavity (ASLOC) structure of the gain chip is designed for weak optical confinement (equivalent vertical spotsize $d/\Gamma = 1.2 \ \mu$m), low optical losses ($\propto 4$ dB/cm) and reduced electron leakage current to enable high-power operation. It consists of n-$Al_{0.35}Ga_{0.65}As$ cladding, 1.6 μm n-$Al_{0.25}Ga_{0.75}As$ confinement, active region, 0.8 μm p-$Al_{0.25}Ga_{0.75}As$ confinement, p-$Al_{0.85}Ga_{0.15}As$ cladding and p-GaAs contact layer. The active region contains a compressively strained InGaAs single quantum well embedded in GaAsP spacer and AlGaAs graded index layers. Figure 2(a) shows the calculated vertical profiles of the refractive index and the waveguide mode assuming lateral uniformity.
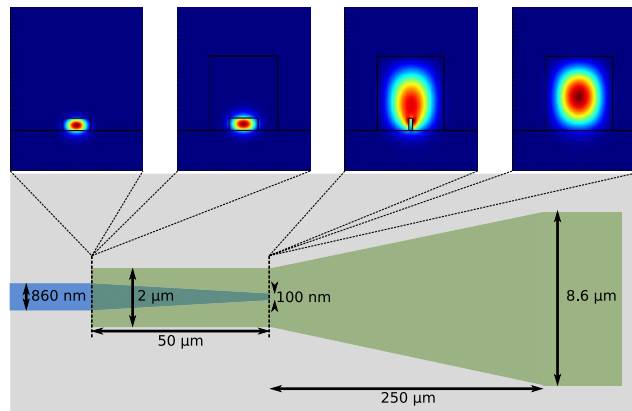
For mode-locking, two-section ridge-waveguide (RW) devices were fabricated from a wafer with the epitaxial layer structure described above by a standard cleanroom process [23]. The width of the ridge is 5 μm and the total gain section length 2000 μm. The saturable absorber section, located at the high-reflection coated rear side of the chip, is 200 μm long. The gain section includes a 1 mm RW bend with a tilt angle of 3° at the anti-reflection coated front facet to avoid parasitic reflections. The electrical isolation between absorber and gain sections is achieved by a 30 μm wide interruption of the metalization and a shallow He$^+$ implantation. To evaluate the electro-optical performance, a single-section RW laser having no bend was operated in pulsed

Fig. 2. (a) Calculated profiles of refractive index squared (blue, right axis) and mode intensity (red, left axis) of the gain chip. (b) Measured total output power versus injection current of a 2 mm long RW laser with as-cleaved facets emitting an 1060 nm. Inset: Vertical profile of the far-field intensity.

mode (pulse length 1 μs, repetition frequency 1 kHz). The reflection on the as-cleaved facet was 30%. The measured results are shown in Fig. 2(b). The threshold current is 22 mA and the slope efficiency 0.87 W/A. The full-width at half maximum of the vertical far-field of 24°, a result of the broadened near-field, also facilitates the coupling into the polymer entrance waveguide.

The external cavity chip is made on an SiN-on-insulator platform using 300 nm thick SiN. The waveguide dimensions for the gain chip dictate the mode-shape in the coupling section between both chips. In order to couple from the gain chip to the external cavity chip efficiently, an SU8 intermediate waveguide has been used on the cavity chip for edge coupling, as demonstrated earlier in [15]. This type of structure was chosen because it allows independent tuning of the horizontal and vertical mode size, without having to change the SiN layer thickness. This allows efficient coupling to the non-circular mode shape of the gain chip. The used waveguide and taper sections are schematically shown in Fig. 3.

Fig. 3. Schematic drawing of the used taper structure for the spot size converter. The blue material is SiN, the green material is SU8. The inset modes show the mode profile at both sides of the abrupt transitions, simulated at 1060 nm.

The waveguide dimensions at the facet were optimized in simulation for optimal coupling to the gain chip, and are 8.6 × 1.8 μm^2, and the waveguide angle is 6.6° to match the beam angle in air. Since this waveguide is highly multimode, the adiabatic transition from SiN to SU8 waveguide was made while the SU8 waveguide was still narrower, at 2 μm, where the SU8

waveguide supported only three TE modes, to prevent coupling to higher order modes. The SU8 was then tapered up to the final dimensions over 250 μm. After fabrication, the achieved thickness of the SU8 layer was 1.6 μm. The structure was resimulated for this thickness. The simulated loss of the entire fabricated coupling structure at 1060 nm is 0.84 dB, 0.36 dB for the overlap losses between the gain chip, 0.18 dB for the fresnel transmission between air and the SU8 waveguide, and 0.30 dB for the SU8-to-SiN transition (simulated using an EME solver). There is no AR coating applied to the SiN chip. This could reduce the coupling loss by another 0.18 dB

After the edge coupling structure, the external cavity contains a spiral waveguide with a length of 3.05 cm to increase the cavity length. The outcoupling mirror is formed by a Sagnac reflector designed for a reflection of 75%. The actual reflectivity after fabrication was determined to be 83%, as explained in the Characterization section.. After the Sagnac reflector, a similar SU8 edge coupler is placed, but with a width of 3.0 μm for optimal coupling to a lensed fiber. The height of this structure is not optimal for coupling to a lensed fiber, because it is made in the same process step as the chip-chip edge coupler. The simulated coupling loss is 0.68 dB.

After fabrication, the waveguide losses were measured by comparing the transmission trough several different lengths of waveguide. The measured losses were 1.26 dB/cm at 1064 nm. This is around the expected value, since single mode waveguides for 1550 nm made using the same process technology have losses of 0.3 dB/cm. Since scattering losses scale with wavelength to the fourth power [24], the calculated losses at 1064 nm would be 0.3 dB/cm $\times(1550/1064)^4 = 1.35$ dB/cm. The waveguide losses add a loss of 3.8 dB to the cavity in a single pass. Between the reflector and the outcoupling section on the cavity chip is 0.5 cm of waveguide, adding an extra outcoupling loss of 0.68 dB.
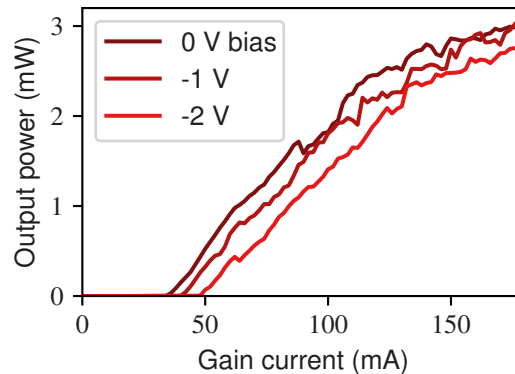
3. Characterization

During characterization of the laser, the active chip was mounted to a small aluminum block, mounted on a Peltier element, with a water-cooled aluminum heatsink. The temperature of the active chip was kept at 20 degrees Celsius during all measurements. The electrical contacting was done through the contact tabs of the C mount. The mount of the active chip was fixed to the optical table. The temperature of the passive chip was not actively controlled.

For butt coupling the passive and the active chip together, the passive chip was placed on a computer controlled XYZ-piezo stage. Using a microscope view from the top, the two chips could be visually aligned. After visual alignment, the alignment was further optimized by maximizing the photocurrent measured in the SA, which is related to the intra-cavity optical power, as long as no mode-locking or Q-switching occurs. Therefore, the alignment was done using a low reverse SA bias of -0.5 V and a gain current slightly above threshold of 65 mA, where only continuous wave (multimode) lasing was observed.

On the fabricated chip, there were also some short cavities. One of these cavities had a threshold current close to that of the chip without external cavity shown in Fig. 2 (25 mA, compared to 22 mA for the as-cleaved chip) when the gain section and SA section were connected in parallel to the current source. The slope efficiency for this laser was 0.064 W/A. Since the threshold current is (almost) the same, the amount of reflection back into the gain chip should be close to the 30% from the as cleaved facet. Using the difference in slope efficiency as well (given by losses including the mirror transmission loss between the gain chip and the outcoupling fiber), two equations with two unknowns can be used to derive the mirror reflection achieved in fabrication and the coupling loss between the active and passive chip. 1 dB coupling loss was added to the simulated value for the lensed fiber coupler, to agree with measurements of test structures, to account for misalignment and fabrication imperfections. Between the outcoupling section and the mirror was 0.9 mm of waveguide, for 1.11 dB of loss. Between the mirror and the gain chip coupling section was 0.2 mm waveguide for 0.25 dB loss, and a theoretical loss of

0.84 dB between the two chips. The extra chip-chip coupling loss was used as a free variable, as well as the mirror reflection. This led to a derived mirror reflectance of 83%, and an extra non-simulated chip-chip coupling loss of 1.15 dB single pass, for a total chip-chip coupling loss of 2.02 dB single pass.
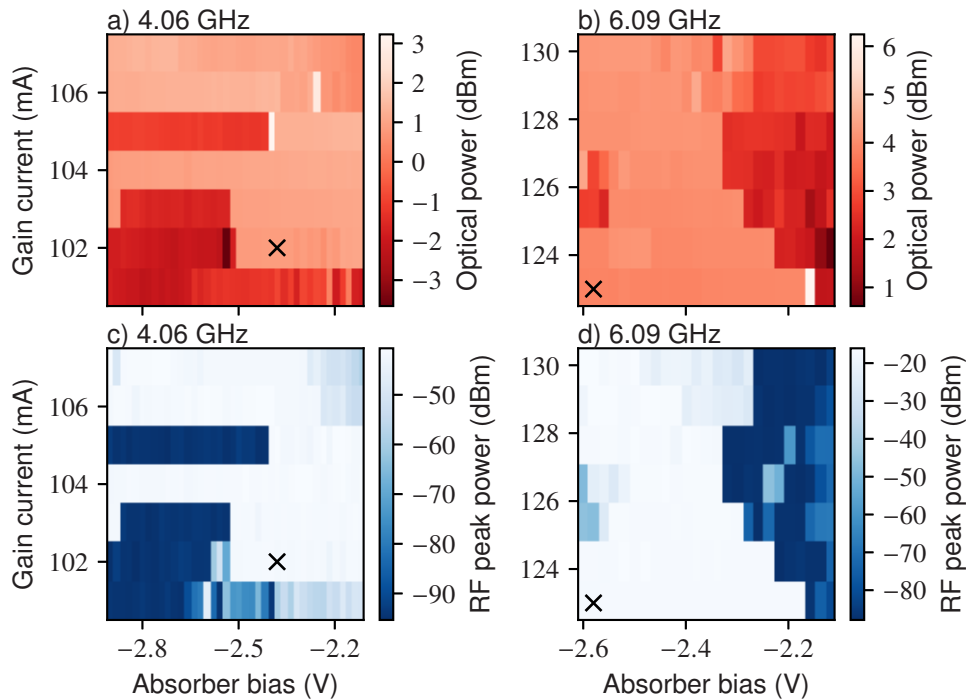
LI curves of the external cavity laser with a longer cavity length (3.05 cm) can be seen in Fig. 4, for SA biases of 0 V, -1 V and -2 V. As expected, the threshold current increases for more negative SA bias. The maximum observed output power in these non-mode-locked operating points is 3 mW.

Fig. 4. LI curves of the laser at SA biases of 0, -1 and -2 V. None of these points were mode-locked operating points.

To find operating points where the laser is mode-locked, a sweep was made over several gain currents and SA biases. The sweep was performed by setting a gain current, and then sweeping the SA bias from the most negative to least negative voltage. Two mode-locking regions were found, one at 4.06 GHz, and one at 6.09 GHz, showing second- and third harmonic mode-locking, respectively. Around the points showing mode-locking, sweeps with smaller steps were performed, which are shown in Fig. 5. No fundamental harmonic mode-locking points were found. It is known, that higher-order harmonic mode locking appears with increasing gain current due to the rise of the unsaturated gain [25]. We think that the absence of fundamental mode locking is caused by a combination of several parameters such as the dependence of the modal gain on the carrier density, the carrier lifetime in the SA and the round-trip time which prevent the existence of a suitable net gain window for fundamental mode locking but still enables higher-harmonic mode locking. The optimal operating conditions for the 4.06 GHz operating point were 102 mA gain current, and -2.38 V absorber bias, while for the 6.09 GHz point it was 123 mA and -2.58 V. The optimal point was chosen as the point with the lowest residual amplitude modulation at 2.03 GHz. The optical output power and RF peak power as a function of the operating point can be seen in Fig. 5. As can be seen, in mode-locked operation, the output power can be higher than the CW measurements shown in Fig. 4. This is because the saturable absorber absorbs less power overall during mode-locked operation. The measured SA current also drops when the laser switches from CW lasing to mode-locked lasing.

Figure 6 shows the optical and RF spectra for the optimal operating point for both second and third harmonic mode-locking. The optical spectra have a 3.8 and 3.9 nm -10 dB bandwidth. It can be seen that for both points the mode-locking is not strictly harmonic, small RF beatnotes can be seen at multiples of the fundamental cavity frequency of 2.03 GHz, but they are at least 35 dB lower than the strongest peaks. This indicates that the pulse train has slight amplitude modulation at the fundamental frequency of 2.03 GHz. The optimal point was chosen where the intensities of these fundamental frequencies were the lowest. The second harmonic mode-locking point
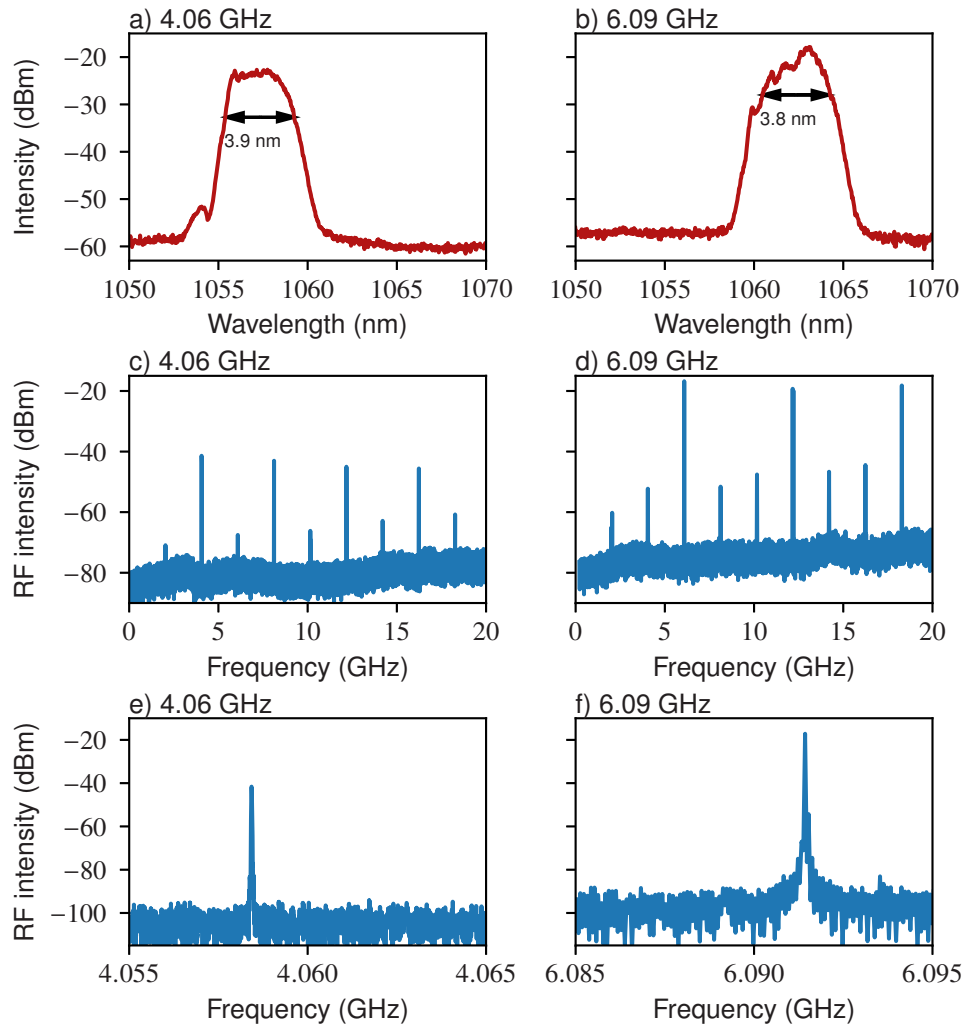
Fig. 5. Mode-locking maps of two operating regions. The crosses show the optimal operating points. (a) shows the optical output power in dBm for the 4.06 GHz operating region, (b) the optical output power in dBm for the 6.09 GHz operating region, (c) the RF peak power in dBm for the 4.06 GHz operating region and (d) the RF peak power in dBm for the 6.09 GHz operating region. The maps were obtained by sweeping the absorber bias from most to least negative voltage for increasing gain currents.

was chosen as the best operating point, because the optical spectrum shows a flat-top, which is useful in for example (dual) frequency comb spectroscopy [26]. The 6 GHz operating point is shown because it is where a secondary laser could be used for optical linewidth measurements described later in this section.

At the 4 GHz operating point, the phase noise of the repetition rate beatnote was measured by measuring the light output using a Discovery DSC10H-39 photodiode, and measuring the RF signal without any amplification with a Keysight N9070A ESA. The result can be seen in Fig. 7. Almost the entire measurement range shows noise that the noise is not Lorentzian shaped (-20 dB/decade), as would be the theoretically expected shape of the repetition rate beatnote [27]. This means the noise that is measured is coming from technical noise sources. It is expected that the main sources are mechanical vibrations slightly changing the distance between both chips, modulating the cavity length and loss, temperature fluctuations, and electrical noise in the output of the laser driver and absorber bias source. An upper limit to the fundamental ASE limited noise linewidth can still be determined from the plot, by finding the highest Lorentzian linewidth that can be put in the graph that doesn't go above the measured noise. This line is given in the plot, and is for a Lorentzian linewidth of 1.7 Hz. It overlaps with the measurement data in the measurement range from 60 Khz until the noise floor starts.

At the 4 GHz operating point, an autocorrelation measurement was done. The output power of the laser was high enough that this was possible without a booster amplifier. the autocorrelation trace can be seen in Fig. 7. A sech^2 pulse shape was fit to the trace, showing a pulsewidth of 6.032 ps. The fourier limited pulsewidth for the spectral width is 335 fs. The pulsewidth
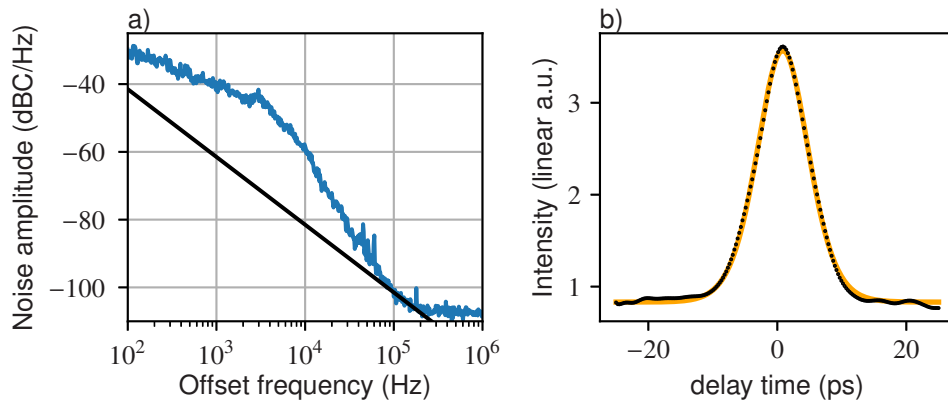
Fig. 6. Spectra measured at the chosen operating points. (a), (c) and (e) are for the 4.06 GHz operating point. (b), (d) and (f) show the 6 GHz operating point. (a) and (b) show the optical spectrum, (c)-(f) show the RF spectrum.
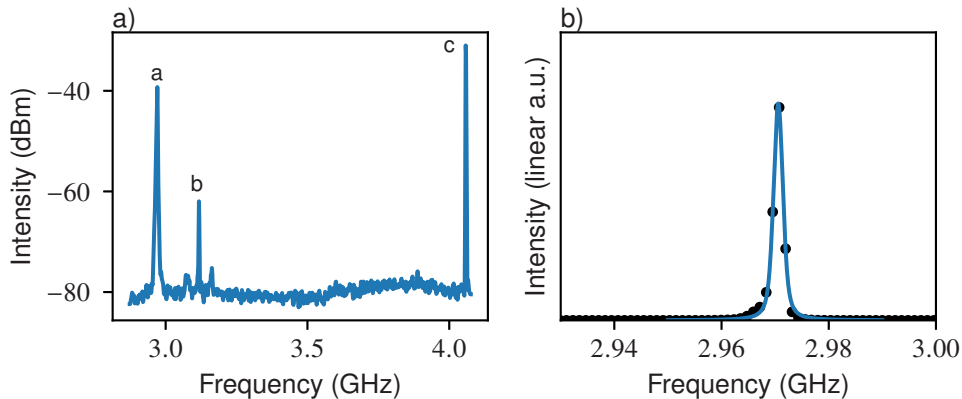
might be slightly broadened due to the dispersion in the 2 meters of fiber between the MLL and the autocorrelator. SMF-28 fiber was used, with a dispersion of -30 ps/nm/km at 1060 nm [28]. multiplying this with a bandwidth of 3.8 nm and fiber length of 2 m leads to a maximum fiber-induced pulse broadening of 0.228 ps.

At the 6 GHz operating point, a single mode laser was available with a wavelength range overlapping with the spectrum of the mode-locked laser. The laser was a Koheras Adjustik Y10 from NKT Photonics with a maximum optical linewidth of 160 kHz FWHM. A heterodyne measurement could be done to estimate the linewidth of the mode-locked laser. The resulting beatnote between the mode-locked laser and fiber laser can be seen in Fig. 8. The Voight fit for this beatnote indicates a linewidth of 4.5 MHz, which is is an upper limit of the optical linewidth of the mode-locked laser. Since this linewidth is an order of magnitude higher than the external laser linewidth, the contribution of the external laser linewidth to this measurement is not significant. The measurement could not be done using a lower resolution bandwidth on the ESA,

Fig. 7. Phase noise and autocorrelation measurement at the 4 GHz operating point. (a) shows the phase noise of the 4 GHz beatnote. (b) shows the autocorrelation measurement (black markers) and the 6.032 ps sech^2 pulse fit to the data (orange line).

because the beatnote frequency was not stable, therefore, the apparent beatnote linewidth would increase with lower resolution bandwidths. This is attributed to the comb spectrum drifting (in both F_{rep} and F_{CEO}) during the longer sweep time for finer resolution bandwidths.
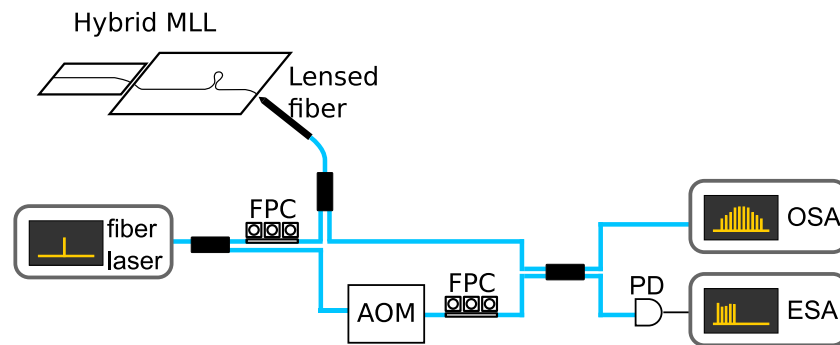

Fig. 8. Measurement of the optical linewidth using a heterodyne measurement with an external fiber laser. (a) Peaks on a large frequency span. Peak a and b are beatnotes between the MLL and the external laser, where a is the beatnote with the 4.06 GHz residual AM peak, and b the beatnote with the lower 2.03 GHz AM peak. Peak c is the 4.06 GHz residual amplitude modulation peak of the MLL (at the 6.09 GHz operating point). The resolution bandwidth is 1 MHz. (b) shows a zoom on peak a from the same trace, with the measured datapoints as black markers, and the Voight shape fit in blue. The measured linewidth is 4.5 MHz. reducing the resolution bandwidth increased the measured linewidth, due to the line drifting during the slower ESA measurement sweep.

Many applications of frequency combs require a comb that is stabilized both in repetition rate F_{rep} as well as carrier envelope offset frequency F_{CEO}. Repetition rate stabilization can be done using hybrid mode-locking, where an RF tone is applied to the SA in addition to the set bias voltage, locking the repetition rate to the RF tone. This is not possible in this laser because the electrical contacts to the SA are large, and therefore have a capacitance too high for RF frequencies to be applied effectively. One of the optical laser lines can be stabilized by using injection locking [29]. This will not stabilize either F_{rep} or F_{CEO}, but it will create a relationship
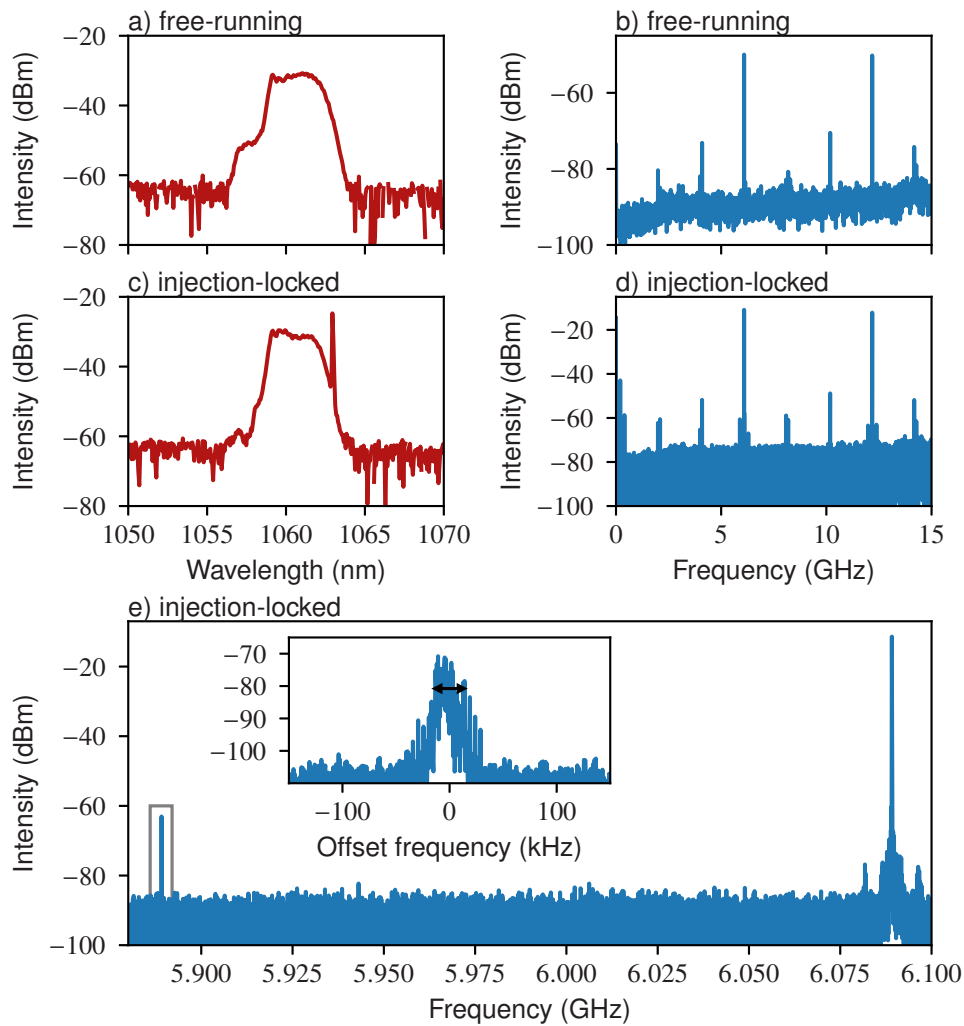
between them. The same fiber laser used for the linewidth measurement was used to demonstrate injection locking. The experimental setup can be seen in Fig. 9. The output of the fiber laser is first split, and one part is sent into the laser output port trough a polarization controller. The other part of the light is frequency shifted using an acousto-optic modulator (AOM) with a modulation frequency of 200 MHz. The frequency shifted laser light is combined with the output of the mode-locked laser before hitting a fast photo-detector. Using the beatnote frequencies measured by the photodetector as feedback, the external laser can be tuned to be close to a laser line in the MLL spectrum. If it gets within the locking range of the MLL, the comb of the MLL will shift to incorporate the external laser line into the comb. In order to measure that the external laser is actually locked to other laser lines in the comb spectrum, a beatnote between the AOM shifted laser line and a second line in the MLL spectrum can be measured. These beatnote will have a frequency of $N \times F_{\text{rep}} \pm F_{\text{AOM}}$. If the beatnote width is lower than the optical linewidth of the free-running laser comb lines, this shows the external laser and comb lines at a different wavelength are also coherent, proving the injection locking has an effect over the entire comb, and not only over the single locked comb line.

Fig. 9. Measurement setup used for the injection locking experiment.

Injection locking experiments were done on the demonstrated laser as well. A slight blueshift was observed in the optical spectrum compared to the operating point for the linewidth measurement. This was attributed to slighly different alignment between both chips. The external laser was set to the lowest possible wavelength of 1062.965 nm, which was the closest possible to the center wavelength of the comb. The power injected from the lensed fiber into the MLL was 1.2 mW. The polarization controller between the external laser and the MLL was optimized to have the highest amount of power in the laser line right after the output port of the splitter at the MLL output, by measuring the peak intensity on an OSA. The other polarization controller was optimized for the highest signal strength on the ESA.

For the demonstrated laser, the injection-locking range was larger than the fine tuning of the external laser (14 pm) The measurements showing injection locking can be seen in Fig. 10. The measurements shown are the optical spectrum and large span RF spectrum with the injection locking laser turned on and off. The optical spectrum narrows slightly when the laser is injection locked. The RF spectra show that the injection locking does not change the mode-locking harmonic, as the laser keeps the same repetition rate. The difference in intensity of the peaks is caused by the extra strong laser line coming directly from the external laser into the PD. Lastly, Fig. 10(e) is a zoom on the RF spectrum showing the repetition rate RF peak and the AOM beatnote in the same measurement. Finally, there's a high resolution zoom on the beatnote between the second comb line and the AOM shifted external laser line, showing a -10 dB width of 28 kHz. This linewidth is significantly narrower compared to the linewidth measured in the heterodyne measurement, showing that the injection locking is working as expected.

Fig. 10. Measurements showing injection locking. (a) shows the optical spectrum at the free-running operating point. (b) shows the RF spectrum at the free running operating point, showing 3rd harmonic mode-locking with some residual amplitude modulation. (RBW 1 MHz) (c) shows the optical spectrum when the laser is injection locked. A part of the red side of the spectrum disappeared. (d) shows the RF spectrum when the laser is injection locked, still showing 3rd harmonic mode-locking, but now additional beatnotes can be seen, caused by the AOM shifted external laser. (RBW 3 MHz) (e) shows the main repetition rate peak, and the beatnote of a comb line with the AOM shifted external laser 200 MHz lower (RBW 11 kHz). The inset shows a high resolution (RBW 3.3 kHz) measurement of that peak, with a measured -10 dB width of 28 kHz, showing coherence between the second comb line and the external laser.

4. Conclusion

The laser in this paper shows that the output power of a hybrid-integrated MLL can be increased by changing the gain chip to one with a higher saturation energy. The MLL also exhibits a low fundamental Lorentzian RF linewidth below 1.7 Hz. Additionally, injection locking could be demonstrated within the comb, both improving the optical linewidth of the comb lines, and fixing

one of the comb lines to a known frequency. This greatly improves the stability of the comb, and if combined with hybrid mode-locking, this would allow the stabilization of both F_{CEO} and F_{rep}. greatly increasing the possible applications for such a comb.

Disclosures. The authors declare no conflicts of interest.

Data availability. No data were generated or analyzed in the presented research.

References

1. J. Nürnberg, B. Willenberg, C. R. Phillips, and U. Keller, "Dual-comb ranging with frequency combs from single cavity free-running laser oscillators," Opt. Express **29**(16), 24910–24918 (2021).
2. I. Coddington, N. Newbury, and W. Swann, "Dual-comb spectroscopy," Optica **3**(4), 414–426 (2016).
3. T. Wilken, G. L. Curto, R. A. Probst, T. Steinmetz, A. Manescau, L. Pasquini, J. I. G. Hernández, R. Rebolo, T. W. Hänsch, T. Udem, and R. Holzwar, "A spectrograph for exoplanet observations calibrated at the centimetre-per-second level," Nature **485**(7400), 611–614 (2012).
4. T. Bajraszewski, M. Wojtkowski, M. Szkulmowski, A. Szkulmowska, R. Huber, and A. Kowalczyk, "Improved spectral optical coherence tomography using optical frequency comb," Opt. Express **16**(6), 4163–4176 (2008).
5. T. Ideguchi, S. Holzner, B. Bernhardt, G. Guelachvili, N. Picqué, and T. W. Hänsch, "Coherent raman spectro-imaging with laser frequency combs," Nature **502**(7471), 355–358 (2013).
6. S. Aumann, S. Donner, J. Fischer, and F. Müller, *Optical Coherence Tomography (OCT): Principle and Technical Realization* (Springer, 2019), pp. 59–85.
7. Y.-K. Min, T. Yamamoto, E. Kohda, T. Ito, and H.-o. Hamaguchi, "1064 nm near-infrared multichannel raman spectroscopy of fresh human lung tissues," J. Raman Spectrosc. **36**(1), 73–76 (2005).
8. K. Van Gasse, S. Uvin, V. Moskalenko, S. Latkowski, G. Roelkens, E. Bente, and B. Kuyken, "Recent advances in the photonic integration of mode-locked laser diodes," IEEE Photonics Technol. Lett. **31**(23), 1870–1873 (2019).
9. L. Chang, S. Liu, and J. E. Bowers, "Integrated optical frequency comb technologies," Nat. Photonics **16**(2), 95–108 (2022).
10. Y. K. Chembo, "Kerr optical frequency combs: theory, applications and perspectives," Nanophotonics **5**(2), 214–230 (2016).
11. A. Rueda, F. Sedlmeir, M. Kumari, G. Leuchs, and H. G. L. Schwefel, "Resonant electro-optic frequency comb," Nature **568**(7752), 378–381 (2019).
12. H. Haus, "Mode-locking of lasers," IEEE J. Sel. Top. Quantum Electron. **6**(6), 1173–1185 (2000).
13. S. Iadanza, A. P. Bakoz, P. K. J. Singaravelu, D. Panettieri, S. A. Schulz, G. C. R. Devarapu, S. Guerber, C. Baudot, F. Boeuf, S. Hegarty, and L. O'Faolain, "Thermally stable hybrid cavity laser based on silicon nitride gratings," Appl. Opt. **57**(22), E218–E223 (2018).
14. A. L. Schawlow and C. H. Townes, "Infrared and optical masers," Phys. Rev. **112**(6), 1940–1949 (1958).
15. E. Vissers, S. Poelman, C. Op de Beeck, K. Van Gasse, and B. Kuyken, "Hybrid integrated mode-locked laser diodes with a silicon nitride extended cavity," Opt. Express **29**(10), 15013–15022 (2021).
16. A. Hermans, K. Van Gasse, J. ø. Kjellman, C. Caër, T. Nakamura, Y. Inada, K. Hisada, T. Hirasawa, S. Cuyvers, S. Kumari, A. Marinins, R. Jansen, G. Roelkens, P. Soussan, X. Rottenberg, and B. Kuyken, "High-pulse-energy iii-v-on-silicon-nitride mode-locked laser," APL Photonics **6**(9), 096102 (2021).
17. S. Cuyvers, B. Haq, C. Op de Beeck, S. Poelman, A. Hermans, Z. Wang, A. Gocalinska, E. Pelucchi, B. Corbett, G. Roelkens, K. Van Gasse, and B. Kuyken, "Low noise heterogeneous III-V-on-silicon-nitride mode-locked comb laser," Laser Photonics Rev. **15**(8), 2000485 (2021).
18. Y. Ibrahimi, S. Boust, Q. Wilmart, J.-F. Paret, A. Garreau, K. Mekhazni, C. Fortin, F. Duport, J.-M. Fedeli, C. Sciancalepore, S. Garcia, and F. van Dijk, "Low FSR mode-locked laser based on InP-Si$_3$N$_4$ hybrid integration," J. Lightwave Technol. **39**(24), 7573–7580 (2021).
19. H. Bastiaens, G. Neijts, A. Memon, Y. Fan, J. Mak, D. Geskus, M. Hoekman, V. Moskalenko, E. Bente, and K.-J. Boller, "Broadband optical frequency comb generation using hybrid integrated InP-Si$_3$N$_4$ diode lasers," in *Conference on Lasers and Electro-Optics Europe and European Quantum Electronics Conference* (IEEE, 2021).
20. Y. Klaver, J. Epping, C. Roeloffzen, and D. Marpaung, "Self-mode-locking in a high-power hybrid silicon nitride integrated laser," Opt. Lett. **47**(1), 198–201 (2022).
21. M. L. Davenport, S. Liu, and J. E. Bowers, "Integrated heterogeneous silicon/III/V mode-locked lasers," Photonics Res. **6**(5), 468–478 (2018).
22. Z. Wang, K. Van Gasse, V. Moskalenko, S. Latkowski, E. Bente, B. Kuyken, and G. Roelkens, "A III-V-on-Si ultra-dense comb laser," Light: Sci. Appl. **6**(5), e16260 (2017).
23. J. Fricke, H. Wenzel, A. Maaßdorf, C. Zink, M. Matalla, R.-S. Unger, and A. Knigge, "Ridge waveguide lasers with vertically stacked quantum wells and tunnel junctions," Semicond. Sci. Technol. **37**(9), 095021 (2022).
24. F. Grillot, L. Vivien, S. Laval, and E. Cassan, "Propagation loss in single-mode ultrasmall square silicon-on-insulator optical waveguides," J. Lightwave Technol. **24**(2), 891–896 (2006).

25. S. Sanders, A. Yariv, J. Paslaski, J. E. Ungar, and H. A. Zarem, "Passive mode locking of a two-section multiple quantum well laser at harmonics of the cavity round-trip frequency," Appl. Phys. Lett. **58**(7), 681–683 (1991).

26. N. Picqué and T. W. Hänsch, "Frequency comb spectroscopy," Nat. Photonics **13**(3), 146–157 (2019).

27. L. Drzewietzki, S. Breuer, and W. Elsäßer, "Timing jitter reduction of passively mode-locked semiconductor lasers by self- and external-injection: Numerical description and experiments," Opt. Express **21**(13), 16142–16161 (2013).

28. N. M. Lüpken and C. Fallnich, "Bandwidth-limited few-cycle pulses by nonlinear compression in a dispersion-alternating fiber," in *Advanced Photonics Congress* (Optica Publishing Group, 2020), paper NpTu1E.2.

29. S. Uvin, S. Keyvaninia, F. Lelarge, G.-H. Duan, B. Kuyken, and G. Roelkens, "Narrow line width frequency comb source based on an injection-locked III-V-on-silicon mode-locked laser," Opt. Express **24**(5), 5277–5286 (2016).